Composite Structures 184 (2018) 428–436

Contents lists available at ScienceDirect

Composite Structures

journal homepage: www.elsevier.com/locate/compstruct

Effect of microchannels on the crashworthiness of fiber-reinforced composites

Stephen J. Pety[a,c], Jia En Aw[b,c], Anthony C. Gendusa[b,c], Philip R. Barnett[b,c], Quinn A. Calvert[b,c], Nancy R. Sottos[a,c], Scott R. White[b,c,*]

[a] Department of Materials Science and Engineering, University of Illinois at Urbana-Champaign, 1304 W Green St., Urbana, IL 61801, USA
[b] Department of Aerospace Engineering, University of Illinois at Urbana-Champaign, 104 S. Wright St., Urbana, IL 61801, USA
[c] Beckman Institute for Advanced Science and Technology, University of Illinois at Urbana-Champaign, 405 N Mathews Av., Urbana, IL 61801, USA

ARTICLE INFO

Keywords:
Microvascular composites
Crashworthiness
Damage triggering
Multifunctional materials

ABSTRACT

The integration of microchannels within structural composites enables a range of multifunctional responses such as thermal management and self-healing. In this work, we investigate how microchannels affect the crashworthiness of the host material. Corrugated panels are fabricated with aligned microchannels (ca. 400 μm diameter) at different channel spacing (10 mm and 1.2 mm), orientation with respect to the loading direction, and alignment with respect to the surrounding fiber-reinforcement. Specific energy absorbed (SEA) is measured by compression testing of samples with a chamfer edge trigger. SEA was preserved within 10% for all test cases. Flat (non-corrugated) panels are also tested to demonstrate that microchannels can serendipitously trigger stable, energy absorbing failure modes that lead to improved crashworthiness. Non-vascular panels without an edge chamfer fail catastrophically when compressed. In dramatic contrast, vascular panels fail in a stable fashion triggered by crack initiation at the microchannels, yielding ca. 10 times more energy absorption.

1. Introduction

Microvascular composites have enabled a variety of multifunctional behaviors including self-healing [1,2], thermal management [3–6], damage sensing [7,8], and electromagnetic modulation [9,10]. However, the presence of vasculature can potentially reduce composite mechanical properties. As recently reviewed by Saeed et al. [11], several studies have characterized how microchannels affect properties such as tensile/compressive strength and stiffness [12–15], fatigue behavior [16], mode 1 and mode 2 fracture toughness [17], low-velocity impact response [18,19], and interlaminar shear strength [20]. Mechanical properties are typically preserved when channel volume fraction is low (< 2%) and channels do not disrupt the continuity or architecture of load-bearing plies.

One property that has not been addressed is the energy absorption of composites in a crash (i.e. crashworthiness), an important design factor for their use in transportation. In a crash, fiber-reinforced composites fail through a combination of compressive failure and splaying (delamination and bending) which leads to material disintegration and high energy absorption [21,22]. The specific energy absorbed (SEA) of carbon-fiber/epoxy composites, i.e. the energy absorbed per unit weight in a crash, ranges from 50 to 100 kJ/kg [23]. For comparison, typical SEA values are ca. 30 kJ/kg for aluminum and ca. 20 kJ/kg for steel [23]. Most of the energy absorbed for a composite derives from compressive failure of the fibers and fracture of the matrix [24]. SEA is increased when using fibers with high compressive strength, or matrices with high interlaminar fracture toughness (which reduces splaying) [25].

Composite crashworthiness is characterized by compressing tubes [26], self-supporting corrugated panels [27–29], or flat panels supported by a fixture [30,31]. Samples are usually manufactured with a damage trigger such as an edge chamfer to prevent catastrophic, low energy-absorbing failure modes such as buckling [32]. Tests are carried out at speeds representative of a crash (ca. 50 km h^{-1}) or under quasi-static loading (1–100 mm min^{-1}) for ease of testing [26]. Quasi-static tests typically provide similar failure modes and SEA values compared to high-speed testing since most thermoset composites are insensitive to strain rate in this regime [33].

While no prior investigations have been performed on how microchannels affect composite crashworthiness, several works report on how channels affect composite compressive strength. Kousourakis et al. [12] compressed carbon/epoxy cross-ply composites with aligned 170 μm–680 μm diameter microchannels at 5 mm interchannel spacing.

* Corresponding author at: Department of Aerospace Engineering, University of Illinois at Urbana-Champaign, 104 S. Wright St., Urbana, IL 61801, USA.
E-mail addresses: pety1@illinois.edu (S.J. Pety), jiaenaw2@illinois.edu (J.E. Aw), gendusa2@illinois.edu (A.C. Gendusa), pbarnet3@tennessee.edu (P.R. Barnett), qcalver2@illinois.edu (Q.A. Calvert), n-sottos@illinois.edu (N.R. Sottos), swhite@illinois.edu (S.R. White).

http://dx.doi.org/10.1016/j.compstruct.2017.09.105
Received 20 July 2017; Received in revised form 25 September 2017; Accepted 29 September 2017
Available online 30 September 2017
0263-8223/

Channels were aligned with the fiber direction in surrounding plies in order to reduce their impact on the natural fiber architecture. Channels oriented with the loading direction caused no reduction in strength for any channel diameter tested. When channels were oriented transverse to the loading direction, a reduction in strength (up to 15%) was attributed to the induced waviness of the surrounding 0° plies and the role of the channels as stress concentrators.

Larger reductions in strength can occur if channels are misaligned with surrounding plies. For example, Huang et al. [13] compressed unidirectional carbon/epoxy composites containing 80 μm–560 μm channels oriented transverse to the fiber (and loading) direction. Strength reduction of 10%–70% was observed, attributed to enhanced ply waviness, channel stress concentration, and the formation of resin pockets around channels. Hartl et al. [14] showed similar strength reductions in simulations of transverse channels in a quasi-isotropic layup. Thus, compressive strength reduces most when channels are oriented transverse to the loading direction, have large diameter, and are misaligned with the fiber direction in surrounding plies.

In this manuscript we report the results of an investigation of the crashworthiness of microvascular carbon/epoxy composites. Two different experimental studies were carried out. First, corrugated cross-ply panels were manufactured containing ca. 400 μm channels at either 10 mm or 1.2 mm interchannel spacing. The 10 mm spacing is representative of microvascular composites used for self-healing [18] and active cooling applications [34], while the 1.2 mm spacing is representative of actively cooled composites designed to operate in hypersonic flight [35]. Crush tests were performed for channels oriented either transverse or longitudinal with the loading direction. The effect of misalignment with the fiber direction of surrounding plies was also investigated. Vascular panels were chamfered and compressed under quasi-static loading to compare failure modes and SEA. Flat (non-corrugated) panels were also tested using a knife-edge fixture. We investigated the use of microchannels to trigger (and guide) failure in a stable fashion to achieve high SEA. Panels were fabricated containing three or five transverse channels located 2 mm from the bottom of the sample, misaligned within surrounding 0° plies. Damage initiation and SEA were compared for samples with no damage trigger, a traditional chamfer trigger, and microchannel triggers.

2. Materials and methods

2.1. Fabrication of corrugated panels with evenly spaced microchannels

A corrugated panel geometry was chosen to allow for compression without buckling (Fig. 1a-b). Dimensions are taken from Grauers et al. [27] and are similar to several other studies on the crashworthiness of corrugated panels [28,29]. Microchannels were incorporated both transverse (Fig. 1c) and longitudinal (Fig. 1d) to the loading direction. Channels were either 400 μm diameter circular channels at a spacing s = 10 mm or 430 μm × 330 μm elliptical channels at s = 1.2 mm. Channel volume fraction was nominally 0.6% for the 10 mm spacing and 4% for the 1.2 mm spacing.

Transverse channels were incorporated in the midplane of a $[90|0_3|90_2]_S$ layup sequence, resulting in channels aligned with the fiber direction of surrounding plies (Fig. 2a). Longitudinal channels were incorporated into two different layup sequences to produce channels both aligned and misaligned with the fiber direction of the surrounding plies. Channels misaligned with surrounding plies were created in the midplane of the same $[90|0_3|90_2]_S$ layup (Fig. 2b). Channels aligned with surrounding plies were created in the midplane of a $[0|90_3|0_2]_S$ layup (Fig. 2c). Note that this case is equivalent to transverse compression of the transverse channel layup (Fig. 2a).

Panels were fabricated with twelve layers of unidirectional carbon fiber prepreg. The prepreg consisted of Cycom 977-3 epoxy and Hexcel 12K IM7 carbon fiber (190 g m^{-2} fiber areal weight, Cytec-Solvay) with a nominal fiber volume fraction of 61%. An aluminum mold with four sets of corrugations was prepared by electrical discharge machining (EDM), and then prepreg was laid over this mold and placed in a vacuum bag using the manufacturer recommended layup.

The vaporization of sacrificial components (VaSC) technique [10,36,37] was used to form microchannels with well-controlled interchannel spacing. Sacrificial preforms of polylactide (PLA) infused with 3 wt% tin oxalate (SnOx) catalyst were placed between the 6th and 7th prepreg layers during layup. PLA fibers of ca. 400 μm diameter (CU Aerospace) were used for s = 10 mm, while 3D-printed PLA strips of ca. 430 μm × 330 μm cross-section were used for s = 1.2 mm. The strips were printed with a TAZ6 fused deposition modeling printer (Lulzbot) using PLA filament (CU Aerospace) extruded at 170 °C through a 0.35 mm diameter nozzle at 500 mm/min speed, 0.38 mm print height, and 60 °C bed temperature.

For samples with transverse channels at s = 1.2 mm, butyl rubber pressure strips (3.2 mm thick, Airtech) were added above the final prepreg layer to provide additional compaction during cure. This step was added since these samples otherwise compacted poorly and contained voids. Laminates were cured in an autoclave at 130 °C for 4 h and 160 °C for 3 h (2 °C min^{-1} ramps) under 640 kPa external pressure and vacuum (ca. 50 torr). Panels were then cut to size using a diamond saw and VaSC treated at 200 °C for 32 h and vacuum (ca. 1 torr) to vaporize the PLA [36].

Channel morphology was characterized using a digital microscope (Keyence VHX-5000). Transverse channels aligned with the fiber direction of surrounding plies packed well within surrounding fibers and showed dimensional stability (Fig. 2d-e). In contrast, longitudinal channels misaligned with the fiber direction of surrounding plies were surrounded by a large resin pocket and were significantly compressed during cure (Fig. 2f-g). Circular (ca. 400 μm) PLA fibers at s = 10 mm gave rise to ca. 600 μm × 300 μm channels with discrete resin pockets (Fig. 2f), while 3D-printed PLA at s = 1.2 mm led to ca. 700 μm × 200 μm channels with continuous resin pockets between channels (Fig. 2g). Longitudinal channels aligned with the fiber direction of surrounding plies had similar morphology to transverse channels (Fig. 2h-i).

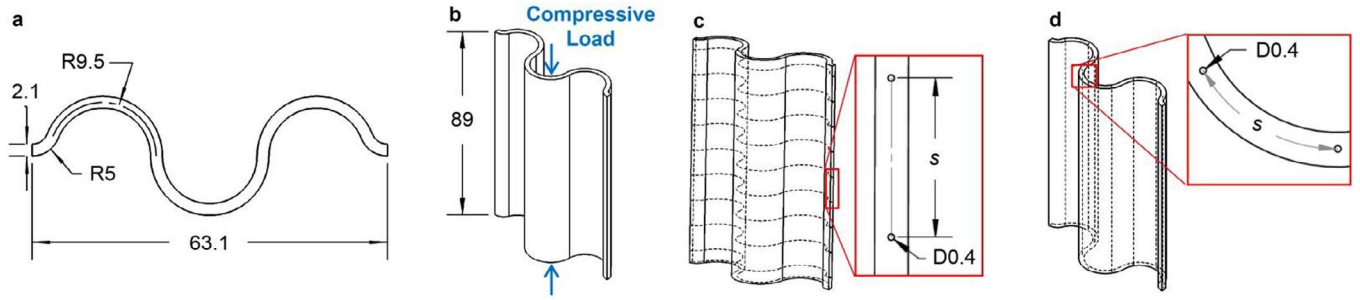

Fig. 1. Geometry of microvascular corrugated panels. a–b) Top and isometric view of panel with dimensions in mm. c–d) Schematics of compression panels with c) transverse and d) longitudinal channel orientations. The channels shown are 0.4 mm diameter with a spacing s of 10 mm. Panels were also fabricated with a denser network of 430 μm × 330 μm channels at s = 1.2 mm.

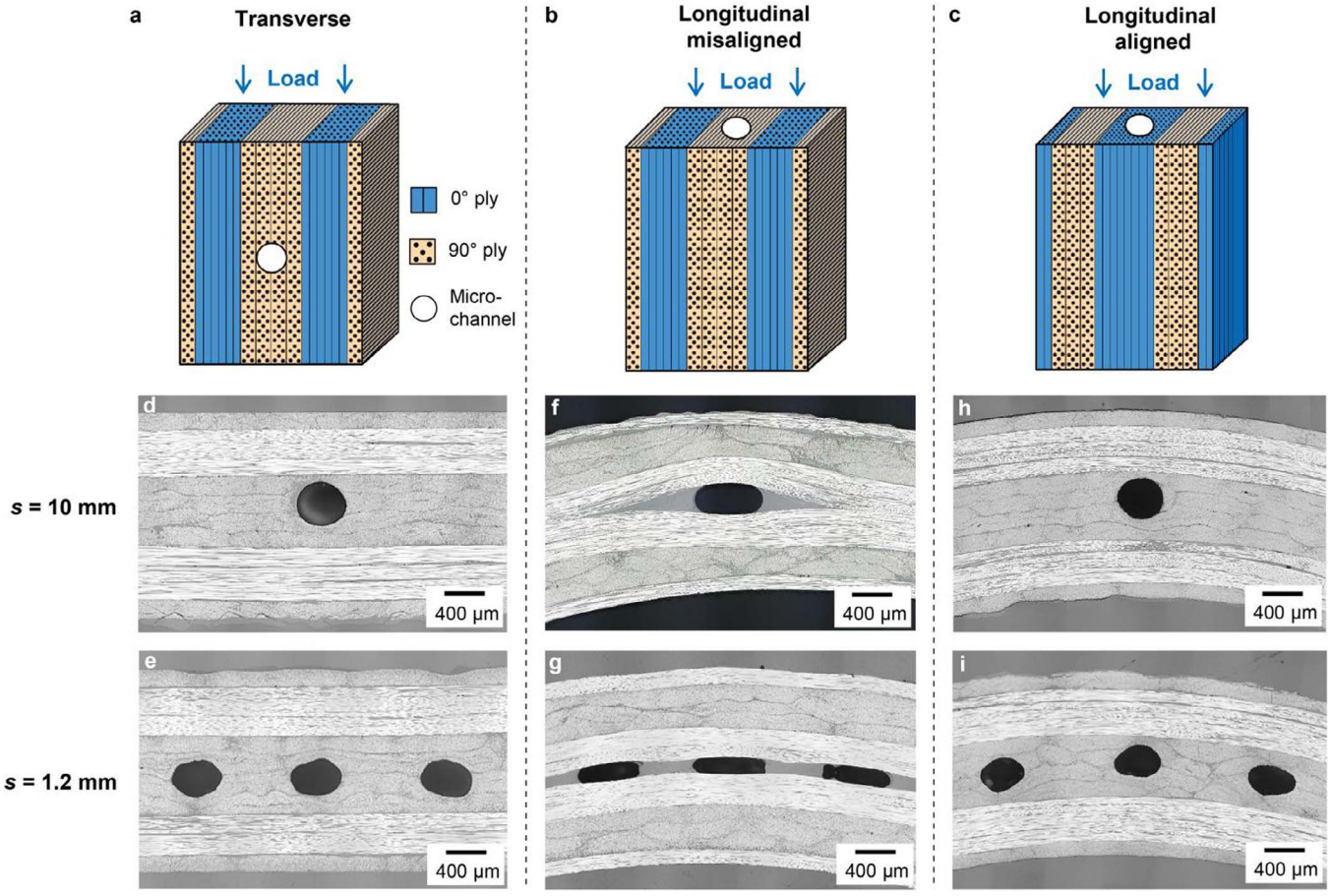

Fig. 2. Layup sequence and channel orientation for microvascular corrugated panels. a) $[90|0_3|90_2]_S$ layup containing transverse channels at the midplane. The channels are aligned with the fiber direction of the surrounding 90° plies. b) The same layup sequence as a) but with longitudinal channels at the midplane. The channels are misaligned with the fiber direction of the surrounding 90° plies. c) $[0|90_3|0_2]_S$ layup containing longitudinal channels at the midplane. The channels are aligned with the fiber direction of the surrounding 0° plies. d–i) Cross-sectional micrographs of samples with channel spacings of 10 mm and 1.2 mm.

2.2. Crush testing of corrugated panels

Panels were sanded with a Dremel on one edge to provide a 45° chamfer for damage triggering (Fig. 3a). Panels were then compressed at 51 mm min^{-1} for a total of 40 mm crosshead displacement in an electromechanical test frame (Instron Model 5984) with a 150 kN load cell (Fig. 3b). Test videos were recorded with a Canon EOS 7D camera. The specific energy absorbed (SEA) of each sample is determined by calculating the average load over a specified crush distance, normalized by the mass crushed, i.e.

$$SEA = \frac{\int_{\delta_1}^{\delta_2} P d\delta}{m_c} = \frac{\overline{P}\,(\delta_2 - \delta_1)}{\rho A L_c} = \frac{\overline{P}\,(\delta_2 - \delta_1)}{m_0/L_0 * L_c} \approx \frac{\overline{P}}{m_0/L_0} \quad (1)$$

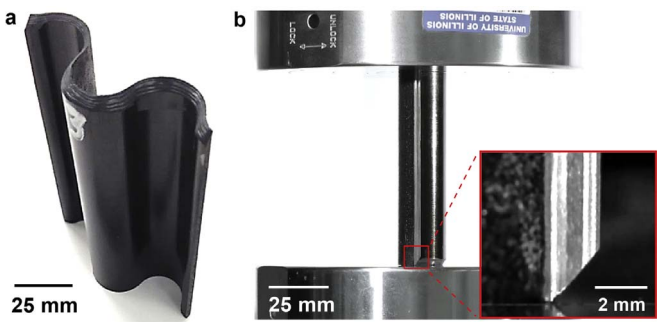

Fig. 3. Crush testing of corrugated panels. a) Image of chamfered sample. b) Panel loaded in compression platens of the Instron test frame.

where P is load, δ is crosshead displacement, $\overline{P}$ is the average load in the analyzed displacement range, m is the sample mass, L is the sample length, and the subscripts $_0$ and $_c$ refer to the original sample state and the amount of the sample that has been crushed, respectively. Steady-state crushing is assumed so that $L_c \approx \delta_2 - \delta_1$. Values of $\delta_1 = 10$ mm and $\delta_2 = 40$ mm were chosen to reflect steady-state behavior independent of the trigger process.

2.3. Statistical analysis of SEA data

A Welch's *t*-test [38] was used to evaluate whether SEA values for vascular samples were significantly different than non-vascular samples. The variance of each sample set s^2 was first calculated as

$$s^2 = \frac{1}{n-1}\sum_{i=1}^{n}(X_i - \overline{X})^2 \quad (2)$$

where n is the number of samples, X_i is the SEA value for a given sample, and $\overline{X}$ is the average SEA value for the set. The t value for comparing vascular samples to non-vascular samples was then calculated as

$$t = \frac{\overline{X_1} - \overline{X_2}}{\sqrt{s_1^2/n_1 + s_2^2/n_2}} \quad (3)$$

where the subscripts 1 and 2 denote the non-vascular and vascular sample sets, respectively. The degrees of freedom f for each comparison were calculated as

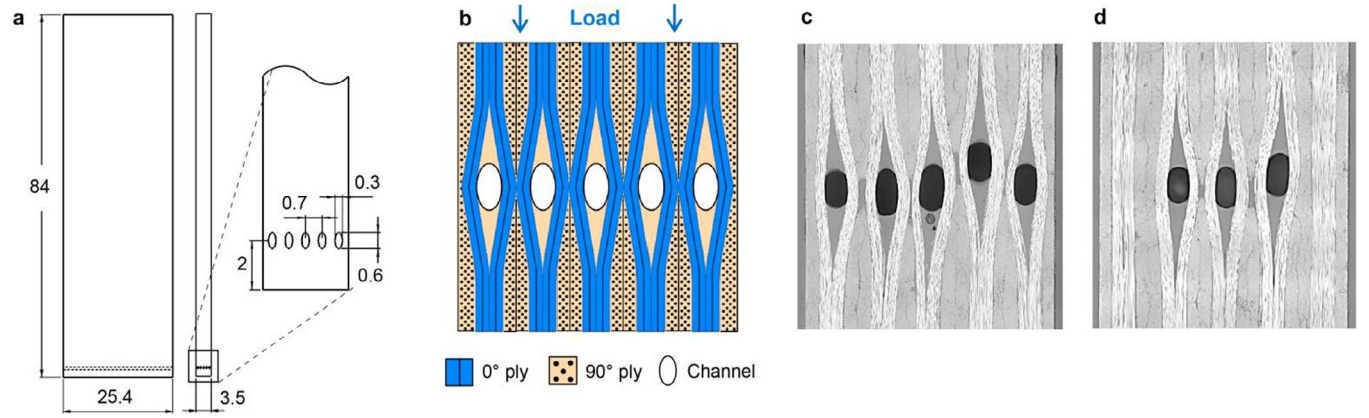

Fig. 4. Geometry and layup sequence of flat microvascular panels for crush testing. a) Panel dimensions (in mm). b) $[90|0_2|90_2|0_2|90_2|0]_s$ layup sequence and channel locations for the five-channel specimens. Samples were also fabricated with only three (middle) channels. c–d) Cross-sectional micrographs of five-channel and three-channel specimens.

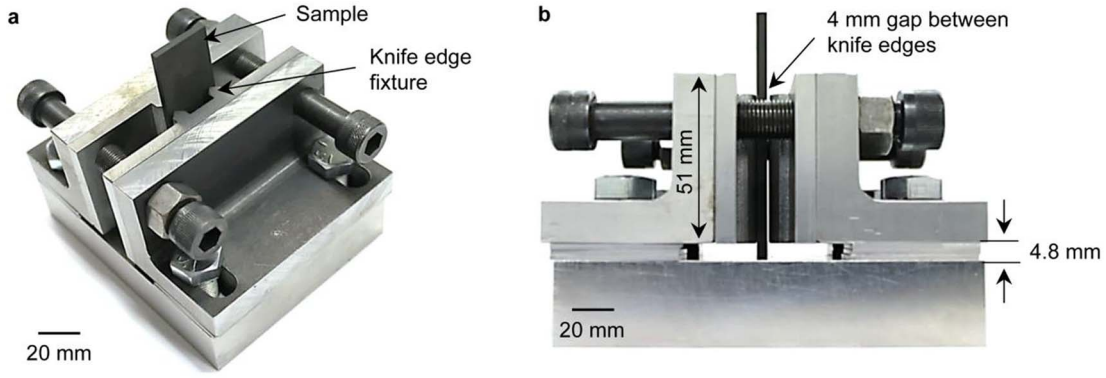

Fig. 5. Knife-edge fixture used for crush testing of flat panels. a) Isometric and b) side views of fixture.

$$f = \frac{(s_1^2/n_1 + s_2^2/n_2)^2}{\frac{s_1^4}{n_1^2(n_1-1)} + \frac{s_2^4}{n_2^2(n_2-1)}}. \quad (4)$$

The values of t and f for each comparison were used to evaluate a p-value for a studentized range distribution. Statistical significance was prescribed for $p < 0.05$. More details on the studentized distribution are found in Salkind [38].

2.4. Fabrication of flat panels with microvascular damage triggers

Flat (non-corrugated) panels were fabricated to investigate the use of microchannels for triggering stable damage modes that lead to high energy absorption. The panel geometry (Fig. 4a) consists of 84 mm × 25.4 mm × 3.5 mm samples with loading along the longitudinal (84 mm) axis. The thickness of the panels was chosen to ensure buckling before compressive failure.

Vascular samples were prepared with either three or five transverse microchannels located 2 mm from the bottom edge of the specimen. Channels were formed by placing 400 μm PLA fibers between the 0° plies of a 20-ply $[90|0_2|90_2|0_2|90_2|0]_s$ layup sequence (Fig. 4b). In order to provide space for embedment of the PLA fibers, 1.2 mm wide strips from surrounding 90° plies were removed which yielded an interior pocket roughly equivalent to the cross-sectional area of the embedded PLA fibers. For five-channel samples, strips aligned with the PLA fibers were excised from all 90° plies except the outermost two. For three-channel samples, strips were excised from all 90° plies except the outermost four.

Panels were fabricated using a flat aluminum mold and the same IM7/977–3 prepreg as corrugated samples. To ensure the alignment of PLA fibers during cure, fibers were pulled through alignment holes in a bracket and held in tension during the cure process. Laminates were cured with the same cure cycle as corrugated samples, cut to oversized dimensions with a diamond saw, and milled to a 84 mm × 25.4 mm final size. The VaSC process (200 °C and vacuum for 16 h) was then performed to yield ca. 600 μm × 300 μm channels with resin pockets (see micrographs in Fig. 4c-d). The incorporation of microchannels also causes fiber waviness in the surrounding 0° plies, further disrupting the load path through the sample.

2.5. Crush testing of flat panels

A knife-edge fixture to support the samples was fabricated based on the design of Ueda et al. [24] and other similar fixtures in the literature [30,31]. The fixture contains knife edges 4.0 mm apart to loosely constrain the 3.5 mm thick samples (Fig. 5). A 4.8 mm region beneath the knife edges allows for locally unconstrained sample crushing. Samples were compressed in this fixture at 3 mm min^{-1} for 15 mm total crush length. SEA was calculated from $\delta_1 = 5$ mm to $\delta_2 = 15$ mm using Eq. (1).

3. Results and discussion

3.1. Crush behavior of corrugated microvascular panels

3.1.1. Crush behavior for transversely aligned microchannels

Crush tests were first performed on control (non-vascular) samples with the layup sequence indicated in Fig. 2a. Non-vascular samples fail through several damage modes as shown in Fig. 6a-b. The 0° plies along the inside radius of the sample corrugations fail by compression (right side of Fig. 6a-b), the middle 90° plies also fail by compression, and the plies along the outer radius of the sample corrugations fail by splaying

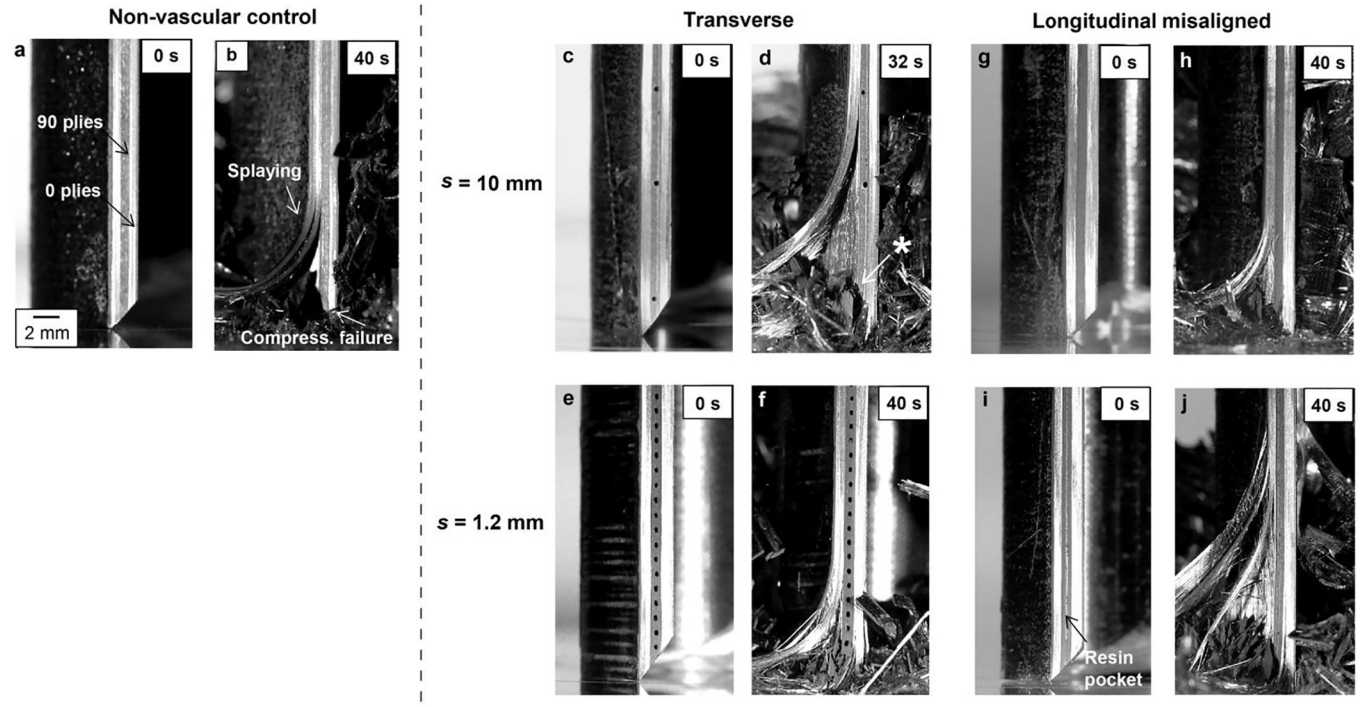

Fig. 6. Crush behavior of corrugated $[90|0_3|90_2]_S$ panels. Test images are shown for a–b) Non-vascular control. c–f) Transverse channels aligned with surrounding plies at spacings of 10 mm and 1.2 mm. The location of a channel-initiated crack is noted (*) in d). g–j) Longitudinal channels misaligned with surrounding plies at spacings of 10 mm and 1.2 mm.

(delamination and bending). These observations are in agreement with reported failure modes for typical cross-ply carbon/epoxy samples [27,28].

Tests were then performed on samples with transverse channels aligned with the fiber direction of surrounding plies. For samples with channels of spacing $s = 10$ mm, the failure mode is largely the same as non-vascular control samples (Fig. 6c-d). However, cracks periodically initiate at the microchannel locations during crush testing, likely the result of stress concentrations. The average delamination length for these samples during crush testing was also ca. 60% higher than non-vascular controls (see Section S1), which is likely due to the channel-initiated cracks that lead to 90° ply debris being pushed farther outward. Vascular samples with $s = 1.2$ mm fail similarly to samples with $s = 10$ mm (Fig. 6e-f), except that smaller pieces of 90° ply debris are created and the delamination length was unchanged compared to the non-vascular controls.

Loading curves for non-vascular samples and vascular samples were similar regardless of channel spacing (Fig. 7a). The loading curves feature an initial linear increase in load as the chamfer is consumed, followed by a region of generally steady crush load. Fig. 7b compares the average SEA values for these samples. Non-vascular control samples have an average SEA of 55 kJ/kg, while vascular samples showed slight reductions in SEA (a 7% reduction for $s = 10$ mm and 10% for $s = 1.2$ mm). A two-tailed t-test reveals that neither of these reductions are statistically significant, with $p = 0.20$ for $s = 10$ mm and $p = 0.06$ for $s = 1.2$ mm (see Table 1).

3.1.2. Crush behavior for longitudinally misaligned microchannels

Samples were also tested using the same layup sequence, but with longitudinal channels misaligned with the fiber direction of surrounding plies (Fig. 2b). Vascular samples with $s = 10$ mm fail qualitatively similarly to non-vascular samples (Fig. 6g-h). Vascular samples with $s = 1.2$ mm also fail similarly (Fig. 6i-j), except with ca. 20% longer delaminations (see Section S1). The increase in delamination length is likely a result of the continuous resin pocket formed in the center of these samples, pushing the surrounding 0° plies farther from the center of the panel and increasing the likelihood of splaying.

Fig. 7b shows that the average SEA for vascular samples with $s = 10$ mm exhibits no significant reduction compared to non-vascular controls ($p = 0.64$). Vascular samples with $s = 1.2$ mm showed a 10% reduction that was statistically significant ($p = 0.04$, see Table 1). This slight reduction in SEA is attributed to the continuous resin pocket, which forces 0° plies farther from the center of the sample and increases splaying. The general preservation of SEA for the vascular $[90|0_3|90_2]_S$ samples is attributed to the placement of channels between the central 90° plies, limiting their influence on the compressive failure of the surrounding 0° (load-bearing) plies.

3.1.3. Crush behavior for longitudinally aligned channels

Finally, samples were also tested with longitudinal channels aligned with the fiber direction of surrounding 0° plies (Fig. 2c). Non-vascular control samples were tested again since the layup sequence was slightly changed. Again, failure occurs through splaying of the outer plies and compressive failure of the middle 0° and 90° plies (Fig. 8a-b). Vascular samples with $s = 10$ mm fail in the same qualitative manner (Fig. 8c-d), as do vascular samples with $s = 1.2$ mm (Fig. 8e-f).

Loading curves for non-vascular and vascular samples were similar (Fig. 9a). Fig. 9b shows that vascular samples showed slight reductions in SEA (5% for both spacings), which were statistically insignificant ($p = 0.33$ and $p = 0.28$, see Table 1). The preservation of SEA is attributed to the fact that these channels are parallel to the load path and their integration does not lead to misalignment of the surrounding 0° plies.

3.2. Use of microchannels to trigger stable failure modes and high energy absorption

Non-vascular (control) flat panel samples were tested in quasi-static compression using the knife edge fixture shown in Fig. 5. Specimens without a chamfer fail by buckling followed by catastrophic splaying failure at the top of the sample (see damage initiation in Fig. S2a-c and crush behavior in Fig. 10a-b). When chamfered, these same specimens fail progressively through the formation of small interlaminar cracks, delaminations, compressive failure of the inner plies, and splaying of outer plies (see Fig. S2d-e and Fig. 10c-d).

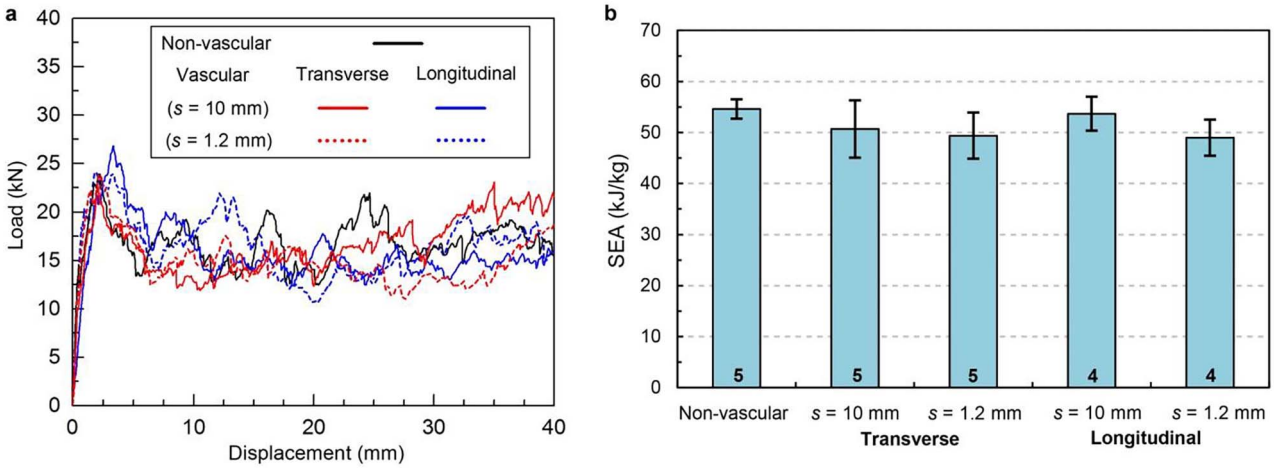

Fig. 7. Energy absorption of corrugated $[90|0_3|90_2]_S$ panels with transverse channels aligned with surrounding plies and longitudinal channels misaligned with surrounding plies. a) Representative loading curves. b) Average specific energy absorbed (SEA). Error bars denote the standard deviation of the data.

Table 1
Average SEA values for all corrugated samples, and *p*-values calculated from Welch's *t*-test statistical analysis. $p < 0.05$ indicates a statistically significant deviation from the non-vascular controls.

Layup	Sample set	Av. SEA (kJ/kg)	Sample number	p
$[90|0_3|90_2]_S$	Non-vascular	54.6	5	N/A
"	Transverse s = 10 mm	50.7	5	0.20
"	Transverse s = 1.2 mm	49.4	5	0.06
"	Longitudinal s = 10 mm	53.7	4	0.64
"	Longitudinal s = 1.2 mm	49.0	4	0.04
$[0|90_3|0_2]_S$	Non-vascular	55.8	5	N/A
"	Longitudinal s = 10 mm	53.1	5	0.33
"	Longitudinal s = 1.2 mm	52.8	5	0.28

Vascular samples of either three-channel or five-channel configuration were tested. For all samples, failure initiated at the microchannels before global buckling and splaying (Fig. S2f-i). Once triggered, damage progressed through compressive failure of inner plies and splaying of outer plies (Fig. 10e-h). Both three-channel and five-channel configurations produced similar failure modes.

Fig. 11a shows representative loading curves for samples with different types of damage triggers. The flat edge sample reaches the highest load before buckling and splaying occurs. The failure stress is approximately 48% of the predicted compressive failure strength of 870 MPa calculated from Tsai-Wu failure theory and manufacturer properties (Fig. 11b). After buckling, the load drops significantly and no further energy absorption occurs. Chamfered samples show a gradual rise to a steady crushing load as the chamfer region is consumed (Fig. 11a). The sustained crushing load is primarily attributed to progressive compressive failure of the 0° plies.

In dramatic contrast, vascular samples show a similar compressive stiffness as flat edge control samples until reaching a critical load at which point cracks initiate at the microchannels. The load drops precipitously, but then recovers to a similar sustained crushing load as chamfered samples. The maximum stress values to initiate damage for three-channel and five-channel samples were 43% and 36% of the compressive strength, respectively (Fig. 11b). The presence of microchannels disrupts the load path (by ply waviness) to initiate damage before the critical buckling load is reached. Once triggered, failure is progressive and stable, consuming large energy.

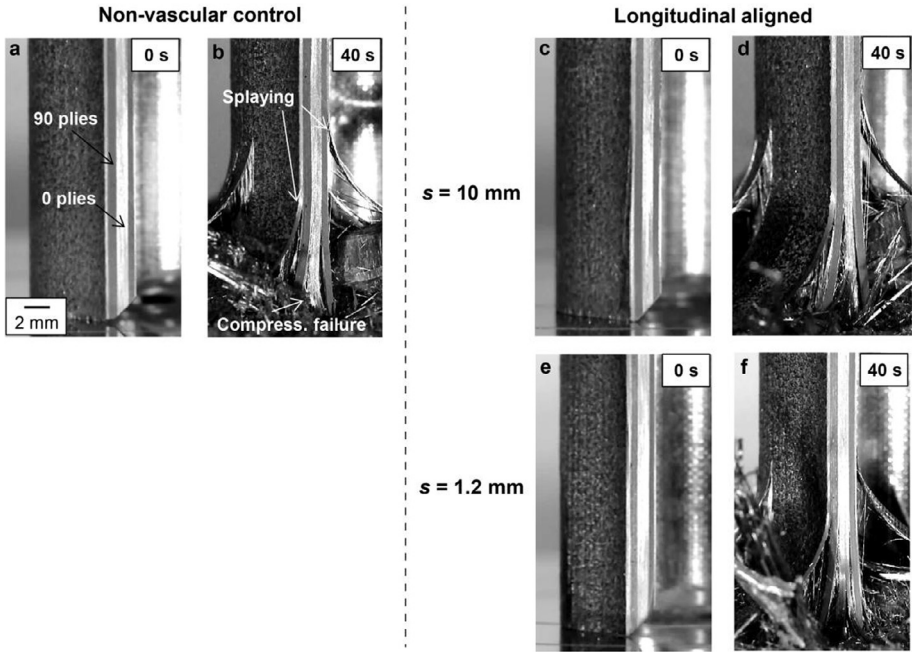

Fig. 8. Crush behavior of corrugated $[0|90_3|0_2]_S$ panels. Test images are shown for a–b) Non-vascular control. c–f) Longitudinal channels aligned with surrounding plies at spacings of 10 mm and 1.2 mm.

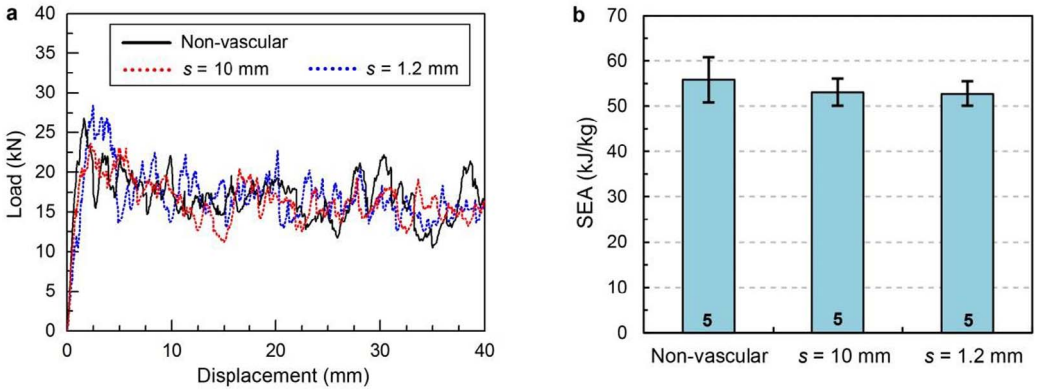

Fig. 9. Energy absorption of corrugated $[0|90_3|0_2]_S$ panels with longitudinal channels aligned with surrounding plies. a) Representative loading curves. b) Average specific energy absorbed (SEA). Error bars denote the standard deviation of the data.

Average SEA values are presented for all types of samples in Fig. 11b. Samples without a trigger have a very low SEA of 2 kJ/kg due to the absence of load recovery after initial splaying. Chamfered and vascular samples show an order of magnitude higher SEA (18–22 kJ/kg). The lower SEA values for flat panel samples (compared to corrugated samples) is due to the lack of hoop constraint in flat panels, leading to increased splaying [26].

Channels are equally effective as chamfers for triggering stable, energy-absorbing damage modes during crushing. Panels with vascular triggers have unique advantages over chamfered panels as well. Vascular panels retain high stiffness before triggering damage, and the critical load can be tuned by channel density and presumably channel size. Pety and coworkers [39] also demonstrated that the critical load is further reduced by cutting 0° plies to make space for channels. The maximum stress values for three-channel and five-channel samples with cut 0° plies were 19% and 10% of the compressive strength, respectively. Finally, vascular panels retain flat faces on both ends which are useful for mating components.

4. Conclusions

The addition of microvascular channels has potential to improve and control the crashworthiness of carbon/epoxy composites. We first investigated the effect of 400 μm diameter channels on the composite material. Corrugated panels were tested with different combinations of interchannel spacing (10 mm or 1.2 mm), channel orientation with the loading direction, and channel alignment with the fiber direction of surrounding plies. There was no statistically significant change in SEA for any of these test cases except for longitudinal channels misaligned with surrounding plies at 1.2 mm spacing, in which a 10% decrease in SEA was measured. Otherwise, the preservation of SEA is attributed to the placement of channels between relatively non-critical 90° plies (for transverse and longitudinal misaligned channels), or to channels being aligned with the loading direction and the fiber direction of surrounding plies (for longitudinal aligned channels). This result is particularly remarkable for the 1.2 mm spacing, which corresponds to a channel volume fraction of 4%.

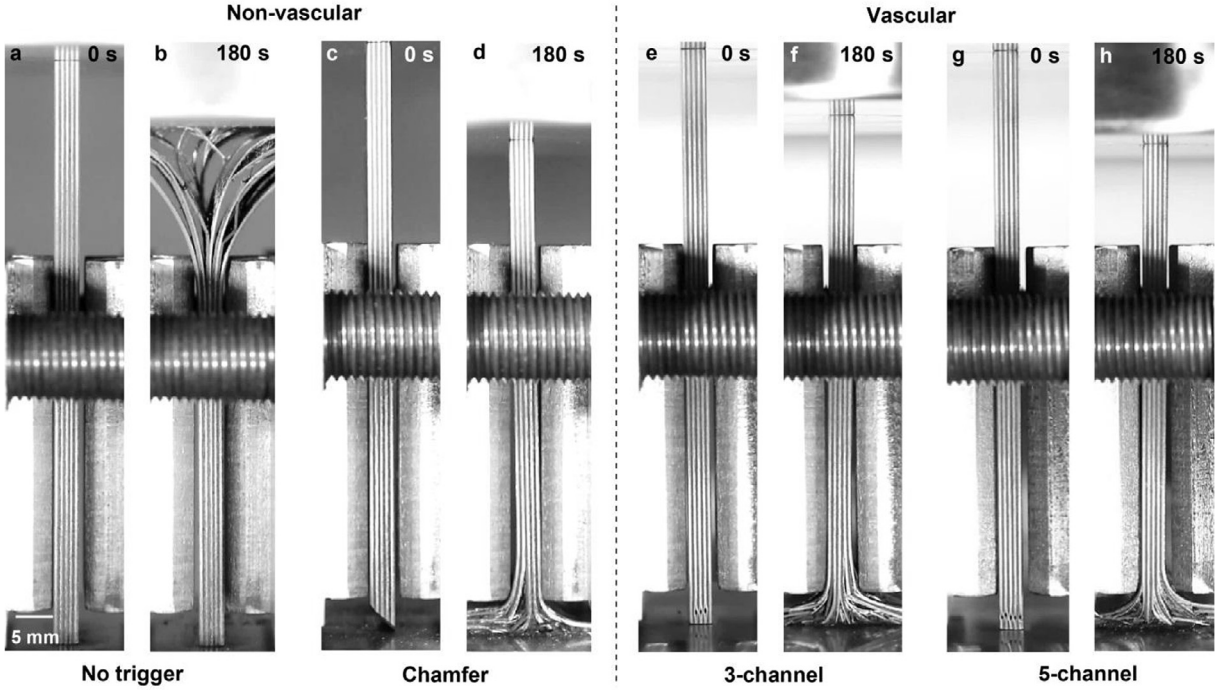

Fig. 10. Crush behavior of flat panels with different damage triggers. Test images are shown for a–b) Non-vascular panel with a flat edge. c–d) Non-vascular panel with a chamfered edge. e–f) Three-channel panel. g–h) Five-channel panel.

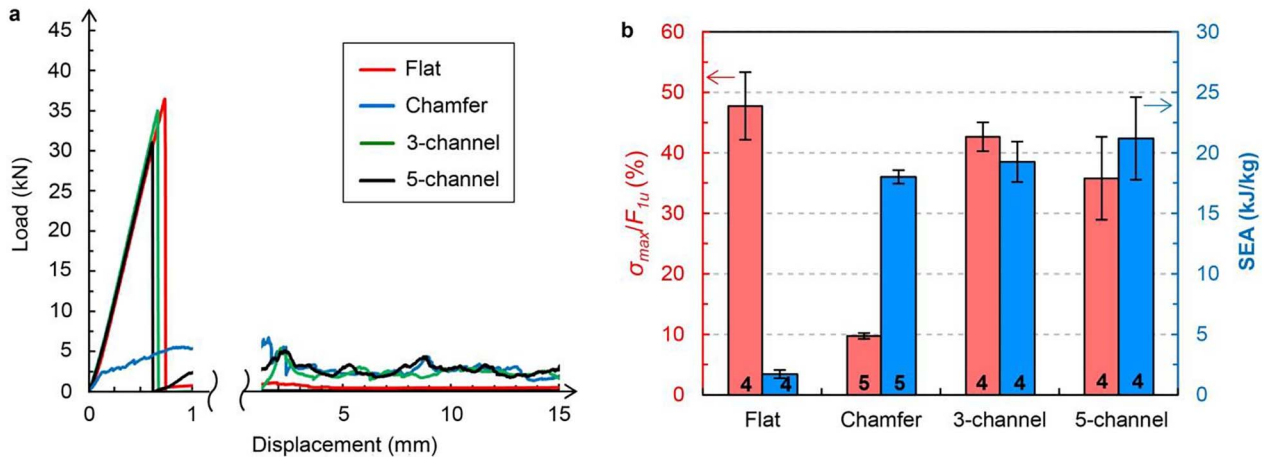

Fig. 11. Crush testing results of flat panel specimens. a) Representative loading curves for panels with a flat edge (no trigger), a chamfer, and either three or five microchannels located 2 mm from the bottom edge. b) Average values of maximum stress normalized by the compressive failure strength (F_{1U} = 870 MPa), and specific energy absorbed (SEA). Error bars denote the standard deviation of the data.

Flat panels were then tested to show that microchannels can enhance crashworthiness by triggering stable, energy-absorbing failure modes. Non-vascular panels without a chamfer buckled, splayed, and had very low SEA. In contrast, panels with three or five microchannels located 2 mm from the bottom of the sample had failure initiate at the channels, progressive and stable failure thereafter, and ca. 10 times higher SEA. Vascular damage triggers were also shown to have advantages over chamfer damage triggers, such as higher stiffness and tunable trigger load. These studies confirm that the incorporation of microchannels (up to 4 vol%) can be achieved in laminated fiber-reinforced composites without sacrificing their crashworthiness through proper specimen design.

Acknowledgements

This research was supported by the National Science Foundation [CMMI 14-36720]. SJP was supported by DoD, AFOSR, National Defense Science and Engineering Graduate (NDSEG) Fellowship, 32 CFR 168a. The authors extend gratitude to Tony Coppola for help with composite manufacturing and testing.

Appendix A. Supplementary data

Supplementary data associated with this article can be found, in the online version, at http://dx.doi.org/10.1016/j.compstruct.2017.09.105.

References

[1] Patrick JF, Robb MJ, Sottos NR, Moore JS, White SR. Polymers with autonomous life-cycle control. Nature 2016;540:363–70.
[2] Hansen CJ. Microvascular-based self-healing materials. Li G, Meng H, editors. Recent Adv. Smart Self-healing Polym. Compos. Cambridge: Elsevier Ltd.; 2015. p. 129–57.
[3] Coppola AM, Griffin AS, Sottos NR, White SR. Retention of mechanical performance of polymer matrix composites above the glass transition temperature by vascular cooling. Compos Part A Appl Sci Manuf 2015;78:412–23.
[4] Coppola AM, Warpinski LG, Murray SP, Sottos NR, White SR. Survival of actively cooled microvascular polymer matrix composites under sustained thermo-mechanical loading. Compos Part A Appl Sci Manuf 2016;82:170–9.
[5] Tan MHY, Najafi AR, Pety SJ, White SR, Geubelle PH. Gradient-based design of actively-cooled microvascular composite panels. Int J Heat Mass Transf 2016;103:594–606.
[6] Pety SJ, Tan MH, Najafi AR, Barnett PR, Geubelle PH, White SR. Carbon fiber composites with 2D microvascular networks for battery cooling. Int J Heat Mass Transf 2017;115:513–22.
[7] Sakurayama N, Minakuchi S, Takeda N. Sensing and healing of disbond in composite stiffened panel using hierarchical system. Compos Struct 2015;132:833–41.
[8] Pang JWC, Bond IP. "Bleeding composites" – Damage detection and self-repair using a biomimetic approach. Compos Part A Appl Sci Manuf 2005;36:183–8.
[9] Hartl DJ, Frank GJ, Huff GH, Baur JW. A liquid metal-based structurally embedded vascular antenna: I. Concept and multiphysical modeling. Smart Mater Struct 2017;26:25002.
[10] Esser-Kahn AP, Thakre PR, Dong H, Patrick JF, Vlasko-Vlasov VK, Sottos NR, et al. Three-dimensional microvascular fiber-reinforced composites. Adv Mater 2011;23:3654–8.
[11] Saeed M, Li B, Chen Z. Mechanical effects of microchannels on fiber-reinforced composite structure. Compos Struct 2016;154:129–41.
[12] Kousourakis A, Bannister MK, Mouritz AP. Tensile and compressive properties of polymer laminates containing internal sensor cavities. Compos Part A Appl Sci Manuf 2008;39:1394–403.
[13] Huang C-Y, Trask RS, Bond IP. Characterization and analysis of carbon fibre-reinforced polymer composite laminates with embedded circular vasculature. J R Soc Interface 2010;7:1229–41.
[14] Hartl DJ, Frank GJ, Baur JW. Effects of microchannels on the mechanical performance of multifunctional composite laminates with unidirectional laminae. Compos Struct 2016;143:242–54.
[15] Coppola AM, Thakre PR, Sottos NR, White SR. Tensile properties and damage evolution in vascular 3D woven glass/epoxy composites. Compos Part A Appl Sci Manuf 2014;59:9–17.
[16] Kousourakis A, Mouritz AP. The effect of self-healing hollow fibres on the mechanical properties of polymer composites. Smart Mater Struct 2010;19:85021.
[17] Norris CJ, Bond IP, Trask RS. Interactions between propagating cracks and bioinspired self-healing vascules embedded in glass fibre reinforced composites. Compos Sci Technol 2011;71:847–53.
[18] Norris CJ, Bond IP, Trask RS. The role of embedded bioinspired vasculature on damage formation in self-healing carbon fibre reinforced composites. Compos Part A Appl Sci Manuf 2011;42:639–48.
[19] McCombe GP, Rouse J, Trask RS, Withers PJ, Bond IP. X-ray damage characterisation in self-healing fibre reinforced polymers. Compos Part A Appl Sci Manuf 2012;43:613–20.
[20] Kousourakis A, Mouritz AP, Bannister MK. Interlaminar properties of polymer laminates containing internal sensor cavities. Compos Struct 2006;75:610–8.
[21] Belingardi G. Energy absorbing sacrificial structures made of composite materials for vehicle crash design. Abrate S, Catanie B, Rajapakse YDS, editors. Dyn. Fail. Compos. Sandw. Struct. New York: Springer; 2013. p. 577–610.
[22] Johnson AF, Thomson RS, David M, Joosten MW. Design and testing of crashworthy aerospace composite components. Irving P, Soutis C, editors. Polym. Compos. Aerosp. Ind. New York: Elsevier Ltd; 2015. p. 261–93.
[23] Barnes G, Coles I, Roberts R, Adams DO, Garner DM. Crash safety assurance strategies for future plastic and composite intensive vehicles, Report Number: DOT-VNTSC-NHTSA-10-01, National Highway Traffic Safety Administration 2010. https://www.nhtsa.gov/DOT/NHTSA/NVS/Crashworthiness/Plastics/DOT-VNTSC-NHTSA-10-01.pdf (accessed February 8, 2017).
[24] Ueda M, Anzai S, Kubo T. Progressive crushing of a unidirectional CFRP plate with V-shaped trigger. Adv Compos Mater 2014:1–11.
[25] Falzon BG, Tan W. Virtual testing of composite structures: progress and challenges in predicting damage, residual strength and crashworthiness. Beaumont PWR, Soutis C, editors. Struct. Integr. Carbon Fiber Compos. Cham: Springer International Publishing; 2017. p. 699–743.
[26] Lukaszewicz DH-JA. Automotive composite structures for crashworthiness. Elmarakbi A, editor. Adv. Compos. Mater. Automot. Appl. Struct. Integr. Crashworthiness Chichester: John Wiley & Sons, Ltd; 2014. p. 99–127.
[27] Grauers L, Olsson R, Gutkin R. Energy absorption and damage mechanisms in progressive crushing of corrugated NCF laminates: fractographic analysis. Compos Struct 2014;110:110–7.
[28] Feraboli P. Development of a corrugated test specimen for composite materials energy absorption. J Compos Mater 2008;42:229–56.
[29] Tan W, Falzon BG. Modelling the crush behaviour of thermoplastic composites.

Compos Sci Technol 2016;134:57–71.
[30] Feraboli P. Development of a modified flat-plate test specimen and fixture for composite materials crush energy absorption. J Compos Mater 2009;43:1967–90.
[31] Cauchi-Savona S, Zhang C, Hogg P. Optimisation of crush energy absorption of non-crimp fabric laminates by through-thickness stitching. Compos Part A Appl Sci Manuf 2011;42:712–22.
[32] Mamalis AG, Manolakos DE, Ioannidis MB, Papapostolou DP. Crashworthy characteristics of axially statically compressed thin-walled square CFRP composite tubes: experimental. Compos Struct 2004;63:347–60.
[33] Courteau MA. Investigating the crashworthiness characteristics of carbon fiber/epoxy tubes. University of Utah; 2011. [Masters thesis].
[34] Pety SJ, Chia PXL, Carrington SM, White SR. Active cooling of microvascular composites for battery packaging. Smart Mater Struct 2017;26:10500.
[35] Soghrati S, Najafi AR, Lin JH, Hughes KM, White SR, Sottos NR, et al. Computational analysis of actively-cooled 3D woven microvascular composites using a stabilized interface-enriched generalized finite element method. Int J Heat Mass Transf 2013;65:153–64.
[36] Gergely RCR, Pety SJ, Krull BP, Patrick JF, Doan TQ, Coppola AM, et al. Multidimensional vascularized polymers using degradable sacrificial templates. Adv Funct Mater 2015;25:1043–52.
[37] Patrick JF, Krull BP, Garg M, Mangun CL, Moore JS, Sottos NR, et al. Robust sacrificial polymer templates for 3D interconnected microvasculature in fiber-reinforced composites. Compos Part A 2017;100:361–70.
[38] Salkind NJ. Encyclopedia of research design. Thousand Oaks: Sage Publications; 2010.
[39] Pety SJ. Microvascular composites as a multifunctional material for electric vehicles. University of Illinois at Urbana-Champaign; 2017. [PhD Thesis].